than 10 mol% has no further influence on the shape-memory properties. After two cycles of UV irradiation, the clear film turned pale yellow, possibly owing to photo-Fries rearrangement[20], but no changes of shape memory properties were observed (Fig. 3). Although the extent of photoreversibility of the photoresponsive chromophores is around 40%, it is likely that partial cleavage of the photoreversible crosslinks on the microscopic level can lead to the changes of macroscopic mechanical properties and to the shape recovery.

Polymers from the IPN polymer system show an R_f of 20–33% and an R_r of more than 88%. Data obtained at 35 °C (Table 1) are not much different from those obtained at 25 °C. During the irradiation process, the temperature of the polymers does not change, indicating that heating is not the trigger of shape-memory behaviour. When the cyclic photomechanical experiment is performed at lower ε_{max} (such as 20%), higher values for R_f are obtained. Large deformation will broadly distribute the photoresponsive groups within the specimen under test and make aggregation of these functional groups difficult, thereby influencing the photo-fixing reactions. The relaxation behaviour of IPN polymer networks was investigated in control tests, in which an IPN polymer film was examined in the cyclic mechanical test under the same conditions but without applying UV light. The extent of relaxation determined from these experiments is about 2% in a test with $\varepsilon_{max} = 20\%$, and 5% for $\varepsilon_{max} = 50\%$.

Relative to thermoresponsive shape-memory polymers, the strain-recovery rate of photoresponsive shape-memory polymers is comparable, but the strain-fixity rate is much lower, because the mechanism is different. In photoresponsive polymers, the amorphous permanent network itself has long and coiled segments between two netpoints. During the programming process, the coiled segments of the chains are stretched and elongated (Fig. 1C). The strain-fixation via light irradiation is due to formation of new chemical netpoints, rather than freezing the stretched chains as in the case of thermoresponsive shape-memory polymers. The elastic contraction of the stretched chain segments accounts for the lower strain-fixity rate of light-induced shape-memory polymers. However, the unique characteristics of the photoresponsive shape-memory polymers enable shape-recovery at ambient temperatures by using remote activation, and could eliminate the temperature constraints of thermoresponsive shape-memory polymers for medical and other applications arising from external sample heating. □

Methods

Synthesis

As an example of the grafted polymer, the synthesis of BHCA(10,2,1) (see Table 1 for nomenclature) is described: a solution of 12.80 g (100 mmol) BA, 2.60 g (20 mmol) HEMA, 2.46 g (10 mmol) HEA-CA, 0.22 g (0.4 mmol) PPG2M560 and 0.05 g azo-isobutyronitril (AIBN) was polymerized between two glass sheets with a Teflon spacer of ~0.5 mm at 80 °C for 12 h. The resulting films were swollen in chloroform to remove the residual monomers. SCAA was synthesized by reacting 4-arm star-poly(ethylene glycol) ($M_n = 2{,}000$, Shearwater Polymers) with an excess of cinnamylidene acetyl chloride in dry THF solution with triethylene amine as the acid receptor.

Cyclic photomechanical and mechanical tests

These were carried out at 25 or 35 °C (selected to be $T > T_g$ and $T > T_{m,SCAA}$, the melting point of SCAA) on a Zwick-Z005, a tensile tester equipped with a 10 N load cell and a thermochamber (model 091250, Climatic Systems Ltd) controlled by a Eurotherm 902-904 unit (Eurotherm Controls Ltd). Films are cut into standard samples (ISO 527-2/1BB, length 32 mm, width 2 ± 0.2 mm). The elongation rate is 10 mm min^{-1}. For photomechanical tests, an optical system consisting of two UV lamps (30 W, Cathodeon) and an optical filter having the ability to split a light beam reaching the filter at an angle of 45° were added to this set-up. While light having wavelength $\lambda > 260$ nm is passing through the filter, light with wavelength $\lambda < 260$ nm is being reflected.

The influence of UV irradiation on the temperature of the polymer film in the Zwick thermochamber was investigated by inserting a digital thermocouple (RS Components) into the polymer film. During a 1.5 h irradiation period with UV light ($\lambda > 260$ nm or $\lambda < 260$ nm) at 25 or 35 °C, the average fluctuation of the polymer temperature is ±0.1 °C.

Received 6 December 2004; accepted 2 February 2005; doi:10.1038/nature03496.

1. Osada, Y. & Matsuda, A. Shape memory in hydrogels. *Nature* **376,** 219 (1995).
2. Liu, C. & Mather, P. T. Thermomechanical characterization of a tailored series of shape memory polymers. *J. Appl. Med. Polym.* **6,** 47–52 (2002).
3. Rousseau, I. A. & Mather, P. T. Shape memory effect exhibited by smectic-C liquid crystalline elastomers. *J. Am. Chem. Soc.* **125,** 15300–15301 (2003).
4. Lendlein, A. & Kelch, S. Shape-memory polymers. *Angew. Chem. Int. Edn Engl.* **41,** 2034–2057 (2002).
5. Wei, Z. G., Sandström, R. & Miyazaki, S. Shape-memory materials and hybrid composites for smart systems: Part I. Shape-memory materials. *J. Mater. Sci.* **33,** 3743–3762 (1998).
6. Koerner, H. *et al.* Remotely actuated polymer nanocomposites—stress-recovery of carbon-nanotube-filled thermoplastic elastomers. *Nature Mater.* **3,** 115–120 (2004).
7. Maitland, D. J. *et al.* Photothermal properties of shape memory polymer micro-actuators for treating stroke. *Lasers Surg. Med.* **30,** 1–11 (2002).
8. Eisenbach, C. D. Isomerization of aromatic azo chromophores in poly(ethyl acrylate) networks and photomechanical effect. *Polymer* **21,** 1175–1179 (1980).
9. Li, M. H. *et al.* Light-driven side-on nematic elastomer actuators. *Adv. Mater.* **15,** 569–572 (2003).
10. Finkelmann, H., Nishikawa, E., Pereira, G. G. & Warner, M. A new opto-mechanical effect in solids. *Phys. Rev. Lett.* **87,** 015501 (2001).
11. Camacho-Lopez, M., Finkelmann, H., Palffy-Muhoray, P. & Shelley, M. Fast liquid-crystal elastomer swims into the dark. *Nature Mater.* **3,** 307–310 (2004).
12. Yu, Y. L., Nakano, M. & Ikeda, T. Directed bending of a polymer film by light. *Nature* **425,** 145 (2003).
13. Ikeda, T. *et al.* Anisotropic bending and unbending behavior of azobenzene liquid-crystalline gels by light exposure. *Adv. Mater.* **15,** 201–205 (2003).
14. Suzuki, A. & Tanaka, T. Phase transition in polymer gels induced by visible light. *Nature* **346,** 345–347 (1990).
15. Juodkazis, S. *et al.* Reversible phase transitions in polymer gels induced by radiation forces. *Nature* **408,** 178–181 (2000).
16. Akabori, S. *et al.* The novel synthesis of photoreversible cyclobutanocrown ethers by the intramolecular photoaddition of α,ω-dicinnamoyl polyethylene glycol derivatives. *Bull. Chem. Soc. Jpn* **60,** 3453–3455 (1987).
17. Tanaka, H. & Honda, K. Photoreversible reactions of polymers containing cinnamylideneacetate derivatives and the model compounds. *J. Polym. Sci. Polym. Chem. Edn* **15,** 2685–2689 (1977).
18. Kim, B. K., Lee, S. Y. & Xu, M. Polyurethanes having shape memory effects. *Polymer* **37,** 5781–5793 (1996).
19. Tobushi, H., Haray, H., Yamaday, E. & Hayashi, S. Thermomechanical properties in a thin film of shape memory polymer of polyurethane series. *Smart Mater. Struct.* **5,** 483–491 (1996).
20. Haddleton, D. M., Creed, D., Griffin, A. C., Hoyle, C. E. & Venkataram, K. Photochemical crosslinking of main-chain liquid-crystalline polymers containing cinnamoyl groups. *Makromol. Chem. Rapid Commun.* **10,** 391–396 (1989).

Supplementary Information accompanies the paper on **www.nature.com/nature**.

Acknowledgements We thank the Bundesministerium für Bildung und Forschung for a BioFuture Award; H.J. is grateful for an AvH fellowship in 1999/2000.

Competing interests statement The authors declare competing financial interests: details accompany the paper on **www.nature.com/nature**.

Correspondence and requests for materials should be addressed to A.L. (Lendlein@gkss.de).

A doubling of the post-perovskite phase boundary and structure of the Earth's lowermost mantle

John W. Hernlund[1], Christine Thomas[3] & Paul J. Tackley[1,2]

[1]*Department of Earth and Space Sciences, and* [2]*Institute of Geophysics and Planetary Physics, University of California, Los Angeles, Los Angeles, California 90095-1567, USA*
[3]*Department of Earth and Ocean Sciences, University of Liverpool, Liverpool L69 3GP, UK*

The thermal structure of the Earth's lowermost mantle—the D″ layer spanning depths of ~2,600–2,900 kilometres[1]—is key to understanding the dynamical state and history of our planet. Earth's temperature profile (the geotherm) is mostly constrained by phase transitions, such as freezing at the inner-core boundary or changes in crystal structure within the solid mantle, that are detected as discontinuities in seismic wave speed and for which the pressure and temperature conditions can be constrained by

experiment and theory. A recently discovered phase transition at pressures of the D″ layer[2–4] is ideally situated to reveal the thermal structure of the lowermost mantle, where no phase transitions were previously known to exist. Here we show that a pair of seismic discontinuities observed in some regions of D″ can be explained by the same phase transition as the result of a double-crossing of the phase boundary by the geotherm at two different depths. This simple model can also explain why a seismic discontinuity is not observed in some other regions, and provides new constraints for the magnitude of temperature variations within D″.

A seismic discontinuity observed in some regions on top of D″ (ref. 5) has previously been ascribed to large thermal gradients caused by subducted oceanic lithosphere, a compositionally distinct layer, or a solid–solid phase transition[6]. Although previous studies lacked knowledge of any phase transition occurring in the mantle at pressures of the D″ region, combined mantle convection and synthetic seismic wave modelling of these potential scenarios suggested that the discontinuity could best be explained by a phase transition having a Clapeyron slope of ~6 MPa K^{-1} (ref. 7). The recent discovery of a phase transition in $MgSiO_3$ perovskite (Pv) to a post-perovskite (pPv) phase at pressures of the D″ layer exhibiting a Clapeyron slope of ~7–10 MPa K^{-1} (refs 3, 4) is remarkably consistent with these earlier findings.

A thermal boundary layer (TBL) is expected to arise in D″ because heat is transferred across the core–mantle boundary (CMB) via thermal conduction, a relatively inefficient heat-transfer mechanism in silicates. The TBL is characterized by an increased geothermal gradient above the CMB that accounts for potential temperature differences between the ambient mid-mantle and the relatively isothermal outermost core. Unlike other known phase transitions in the Earth's interior, the large Clapeyron slope estimated for the pPv phase boundary combined with the large thermal gradients expected in a TBL can allow the phase boundary to be crossed by the geotherm at two depths. The pPv phase boundary temperature at CMB pressure (136 GPa) has been estimated to be ~4,000 K (refs 3, 4), while CMB temperatures estimated from the melting point of iron at the inner-core boundary span a range between ~3,700 K (ref. 8) and ~4,400 K (ref. 9). The higher core temperature estimates therefore place the lowermost D″ layer within the Pv stability field, whereas the lower estimates predict that pPv is the dominant phase throughout D″ (Fig. 1a).

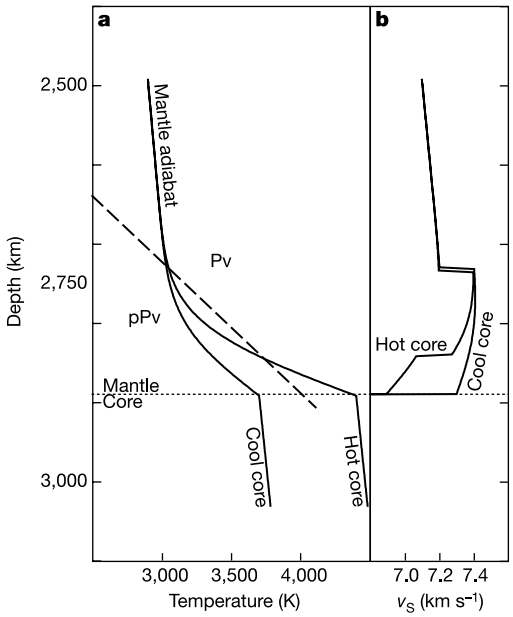

Figure 1 The relationship between the geotherm and pPv phase boundary for different core temperatures (**a**), and corresponding seismic shear-wave profiles (**b**). The geotherms (solid lines in **a**) are plotted following an average mantle adiabat above D″ (ref. 13) with CMB temperatures of 3,700 K (ref. 8; cool core) and 4,400 K (ref. 9; hot core) with the estimated pPv phase boundary (dashed line) superimposed[3]. The v_S profiles in **b** are calculated assuming a constant $\partial v_S/\partial T$ of 0.3 m s^{-1} K^{-1} (ref. 18) for both phases, a v_S increase of 0.2 km s^{-1} in the pPv phase at all depths[6], and an adiabatic variation of v_S referenced to the Preliminary Reference Earth Model[19] and a model geotherm[13] at a height of 320 km above the CMB.

Although estimates of the CMB temperature and pPv phase boundary are likely to remain controversial, only the relative differences between these values at the CMB are important in distinguishing the observational consequences of these two scenarios. We call these the single- and double-crossing models, according to the number of times the geotherm intersects the pPv phase boundary. If the pPv phase is to account for the shear-wave velocity (v_S) increase of 2.5–3% that is required to explain the discontinuity on top of D″ (refs 5, 6), then the v_S profiles for a single- or double-crossing will be very different (Fig. 1b). In particular, the double-crossing model predicts the occurrence of two seismic discontinuities of opposite polarity in D″, and an increased overall gradient in seismic velocities in the lowermost TBL. The single-crossing model, on the other hand, predicts a single ubiquitous global discontinuity at the top of D″.

Recently, seismic migration techniques applied to the D″ layer have revealed a pair of oppositely polarized discontinuities beneath Eurasia[10] and the Caribbean region[11], in good agreement with the predictions of the double-crossing model. The upper discontinuity coincides with a previously detected discontinuity on top of D″ in both regions[5,10–11]. Accordingly, we propose a new paradigm for the gross discontinuity structure of D″ in terms of the double-crossing model (Fig. 2a). v_S profiles corresponding to three scenarios illustrate how variations in discontinuity depth relate to variations in mantle temperature (Fig. 2b). Cold mantle temperatures give rise to a thick pPv stability field, whereas a warm mantle causes it to become smaller in extent, and a pPv layer may be entirely absent if mantle temperatures are higher than the pPv transformation temperature at all depths (Fig. 2c). This mechanism suggests a simple explanation for the absence of a seismic discontinuity in some regions[6].

To test the feasibility of explaining the observed double discontinuity structure with the double-crossing model, we have computed synthetic reflectivity seismograms[12] for the three cases of cold, warm and hot mantle shown in Fig. 2b. In conducting the synthetic tests, we have assumed that the variation of v_S with pressure and temperature are the same in both phases; however, differences are to be expected. Unequal variations should lead to a dependence of discontinuity strength on the depth at which it occurs, but no such correlation is apparent from previous seismic studies spanning a large range of depths (>300 km) for the upper discontinuity[6], and therefore this assumption should not significantly affect the results. For comparison, we use data for an event (8 April 1999, at 43.61° N, 130.35° E, depth of 565 km) recorded by the German Regional Seismic Network (GRSN) with corresponding CMB bounce points beneath Eurasia (65° N, 80° E). The data were filtered with a bandpass of 3–50 s to facilitate comparison with the synthetics, which have a dominant period of 5 s.

The synthetic traces for the cold and warm mantle profiles show clear precursors to the core-reflected ScS phase owing to the upper discontinuity (Fig. 3). In the cold mantle case, a weaker intermediate arrival is present only when the lower discontinuity is included in the model, and this phase is also visible in the real data. This intermediate arrival becomes weaker as mantle temperatures are increased, and the pPv layer becomes thinner. To recover the lower discontinuity in both the cold and warm mantle cases, we have migrated both the synthetic and real data using the same methods as in previous studies[10,11] (Fig. 4). The results of the synthetic tests

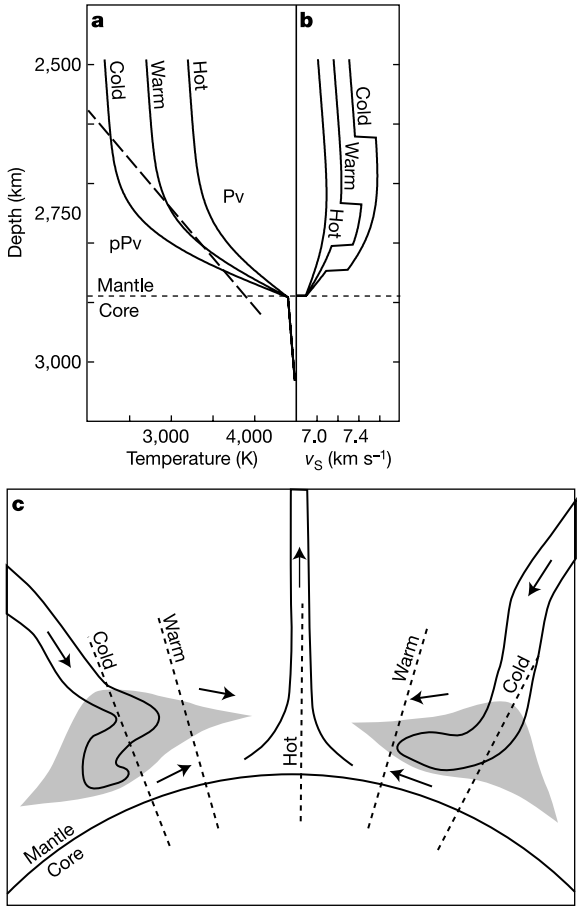

Figure 2 The relationship between three schematic geotherms and the pPv phase boundary (**a**), corresponding v_S profiles (**b**), and a sketch of possible lower-mantle structures (**c**). The v_S profiles are calculated as in Fig. 1b. In **c**, the pPv layer is shown in light grey, schematic flow directions are indicated by arrows, and several examples of warm, cold and hot mantle profiles are shown (dotted lines).

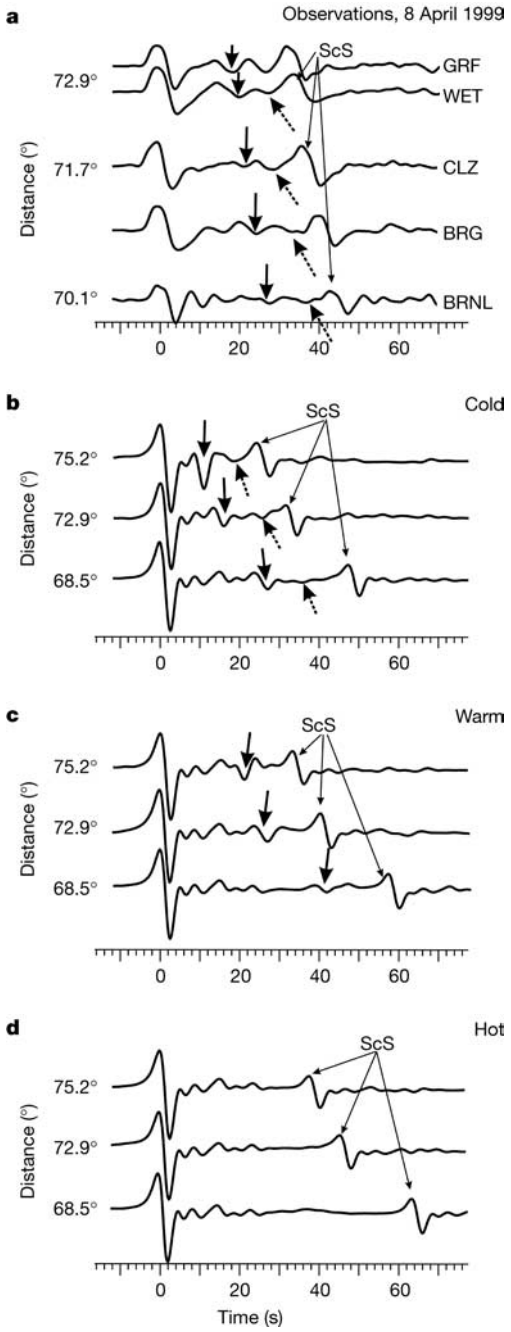

Figure 3 Comparison of data (**a**) with synthetic shear-wave seismograms calculated for the cold (**b**), warm (**c**), and hot (**d**) v_S profiles shown in Fig. 2b. The model is interpolated to match Earth model ak135[20] at depths shallower than 1,000 km, and assumes a density jump of 1% in pPv (refs 2–4). The times are relative, with the traces aligned on the peak of the S phase. The arrival of the core-reflected ScS phase is indicated, the reflection from the upper discontinuity (solid arrows) is shown for the data, cold-mantle and warm-mantle scenarios, and the intermediate arrival attributed to the lower discontinuity (dashed arrows) is shown for the data and cold-mantle scenario.

show that the observed double discontinuity structure is consistent with the double-crossing model. They also indicate that the lower discontinuity will be more difficult to detect in regions where the pPv layer is thin, whereas the upper discontinuity will produce a stronger reflected arrival in all cases. This can explain the lack of a visible lower discontinuity in a portion of the Caribbean region where an upper discontinuity is detected[11].

The double-crossing model provides a framework for constraining the magnitude of temperature variations in regions where a D″ discontinuity exists. For example, a Clapeyron slope of 7–10 MPa K^{-1} translates to a phase boundary gradient of 6–8 K km^{-1} in D″, which must be a lower bound on the radial temperature gradient in order for a double-crossing to occur (Fig. 2a). A thermal conductivity of 10 W m^{-1} K^{-1} (ref. 13) thus yields a minimum conductive heat flux in the range 60–80 mW m^{-2}, similar to values at the Earth's surface in tectonically active regions. If the thermal gradient is not significantly smaller than this phase boundary gradient even in regions where a double-crossing does not occur, the phase relations predict a global CMB heat flow of the order of 9–13 TW. This rate of cooling is probably more than sufficient to power the dynamo in the outer core that is responsible for producing Earth's magnetic field[14,15].

Beneath Eurasia a topographic variation of 55–85 km and 206–316 km above the CMB is observed for the respective lower and upper discontinuities, whereas in the Caribbean region the topographic variations are considerably larger: 66–286 km and 126–416 km above the CMB. The topographic variations imply large lateral temperature gradients along the upper discontinuity of 700–900 K beneath Eurasia and 1,300–1,700 K beneath the Caribbean. These lateral temperature variations are comparable to the expected average temperature change over the TBL, and might be difficult to explain without considering the presence of subducted oceanic lithosphere in both regions. Subducted oceanic lithosphere is expected to exist in both locations if sinking slabs penetrated to the base of Earth's mantle[16]. However, other mechanisms for producing the same change in discontinuity depth need to

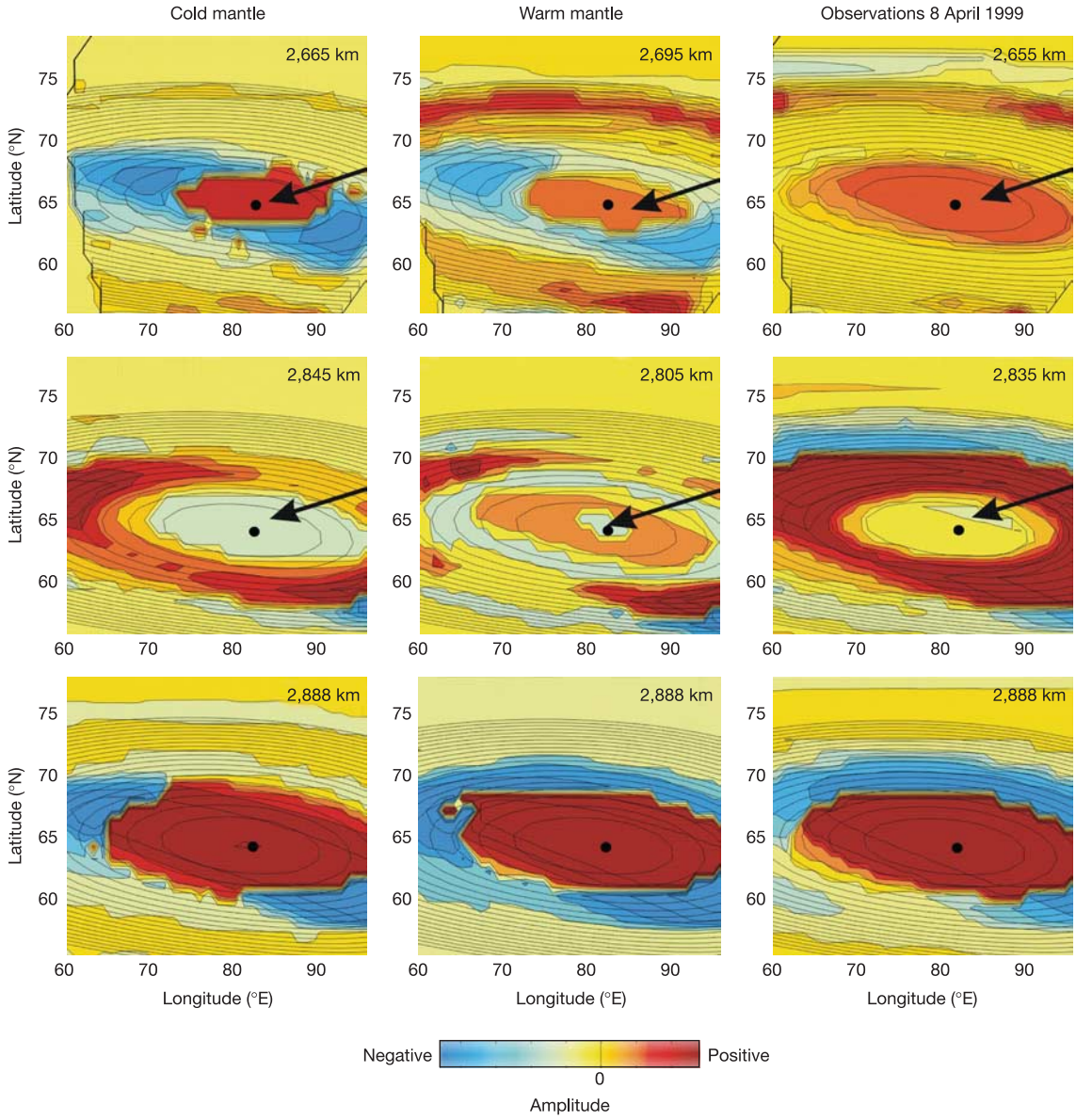

Figure 4 Summary of the migration results for the synthetic cold-mantle (left column) and warm-mantle (centre column) v_S profiles along with real data (right column) using the traces shown in Fig. 3. The discontinuity at the top of D″ is found at two different depths in agreement with the predictions (top row). The deeper discontinuity and its predicted depth can be recovered in all cases (middle row), but is weaker in the warm mantle. The bottom row shows the migrated core-reflected ScS wave. The colour scale represents the relative amplitude of the migration for each case.

be considered before taking this as conclusive evidence for whole-mantle circulation of subducted lithosphere.

The dynamical consequences of a pPv transition at the top of D″ have already been explored in mantle convection models, where an increased convective instability of the lower TBL has been observed[17]. In a double-crossing scenario, the greater vertical extent of the pPv layer in cold regions will increase the relative column density of the mantle in D″ and should provide additional negative buoyancy for cold downwellings such as subducting slabs of oceanic lithosphere. A ~1% density increase associated with the pPv transition[2–4] might be comparable in magnitude to thermal density changes, and should significantly increase the strength of plate-scale circulation in D″.

The effects of a two-phase region, due to the presence of iron and aluminium in Pv plus latent heat associated with a dynamical transition, would transform the discontinuity into a gradient, and might change the effective depth/pressure of the phase transition relative to pure $MgSiO_3$. Iron is expected to induce a two-phase region in the phase diagram, in particular because Fe_2O_3 assumes a structure similar to $MgSiO_3$-pPv at lower pressures[3], but the effects of other chemical components and phases are still largely unknown. A gradient thickness as large as 75 km for the discontinuity on top of D″ is compatible with most seismic studies[6], so we expect the observable effects of a two-phase region to be contained within a corresponding pressure interval of ~4 GPa or less. □

Received 27 September 2004; accepted 15 February 2005; doi:10.1038/nature03472.

1. Bullen, K. E. Compressibility-pressure hypothesis and the Earth's interior. *Mon. Not. R. Astron. Soc. Geophys. Suppl.* **5,** 355–368 (1949).
2. Murakami, M., Hirose, K., Sata, N., Ohishi, Y. & Kawamura, K. Phase transition of $MgSiO_3$ perovskite in the deep lower mantle. *Science* **304,** 855–858 (2004).
3. Oganov, A. R. & Ono, S. Theoretical and experimental evidence for a post-perovskite phase of $MgSiO_3$ in Earth's D″ layer. *Nature* **430,** 445–448 (2004).
4. Tsuchiya, T., Tsuchiya, J., Umemoto, K. & Wentzcovitch, R. M. Phase transition in $MgSiO_3$ perovskite in the earth's lower mantle. *Earth Planet. Sci. Lett.* **224,** 241–248 (2004).
5. Lay, T. & Helmberger, D. V. A shear velocity discontinuity in the lower mantle. *Geophys. Res. Lett.* **10,** 63–66 (1983).

6. Wysession, M. *et al. The Core-Mantle Boundary Region* 273–298 (American Geophysical Union, Washington, DC, 1998).
7. Sidorin, I., Gurnis, M., Helmberger, D. V. & Ding, X. Interpreting $D^{\prime\prime}$ seismic structure using synthetic waveforms computed from dynamic models. *Earth Planet. Sci. Lett.* **163,** 31–41 (1998).
8. Boehler, R. High-pressure experiments and the phase diagram of lower mantle and core constituents. *Rev. Geophys.* **38,** 221–245 (2000).
9. Alfè, D., Gillan, M. J. & Price, G. D. Composition and temperature of the Earth's core constrained by combining ab initio calculations and seismic data. *Earth Planet. Sci. Lett.* **195,** 91–98 (2002).
10. Thomas, C., Kendall, J. & Lowman, J. Lower-mantle seismic discontinuities and the thermal morphology of subducted slabs. *Earth Planet. Sci. Lett.* **225,** 105–113 (2004).
11. Thomas, C., Garnero, E. J. & Lay, T. High-resolution imaging of lowermost mantle structure under the Cocos plate. *J. Geophys. Res.* **109,** B08307 (2004).
12. Müller, G. The reflectivity method: A tutorial. *Z. Geophys.* **58,** 153–174 (1985).
13. Stacey, F. *Physics of the Earth* 3rd edn, appendix G (Brookfield, Kenmore, Queensland, 1992).
14. Buffett, B. A. Estimates of heat flow in the deep mantle based on the power requirements for the geodynamo. *Geophys. Res. Lett.* **29,** GL014649 (2002).
15. Christensen, U. R. & Tilgner, A. Power requirement of the geodynamo from ohmic losses in numerical and laboratory dynamos. *Nature* **429,** 169–171 (2004).
16. Lithgow-Bertelloni, C. & Richards, M. A. The dynamics of Cenozoic and Mesozoic plate motions. *Rev. Geophys.* **36,** 27–78 (1998).
17. Nakagawa, T. & Tackley, P. J. Effects of a perovskite-post perovskite phase change near the core-mantle boundary in compressible mantle convection. *Geophys. Res. Lett.* **31,** L16611 (2004).
18. Aizawa, Y. *et al.* Temperature derivatives of elastic moduli of $MgSiO_3$ perovskite. *Geophys. Res. Lett.* **31,** L01602 (2004).
19. Dziewonski, A. M. & Anderson, D. L. Preliminary reference earth model. *Phys. Earth Planet. Inter.* **25,** 297–356 (1981).
20. Kennett, B. L. N., Engdahl, E. R. & Buland, R. Constraints on seismic velocities in the Earth from travel times. *Geophys. J. Int.* **122,** 108–124 (1995).

Acknowledgements This collaboration was facilitated by the Meeting of Young Researchers in the Earth Sciences (MYRES) held in La Jolla, California, in August 2004. This work was supported by a grant from IGPP Los Alamos.

Competing interests statement The authors declare that they have no competing financial interests.

Correspondence and requests for materials should be addressed to J.W.H. (hernlund@ess.ucla.edu).

Permian tetrapods from the Sahara show climate-controlled endemism in Pangaea

Christian A. Sidor[1], F. Robin O'Keefe[1], Ross Damiani[2], J. Sébastien Steyer[3], Roger M. H. Smith[4], Hans C. E. Larsson[5], Paul C. Sereno[6], Oumarou Ide[7] & Abdoulaye Maga[7]

[1]*Department of Anatomy, New York College of Osteopathic Medicine, Old Westbury, New York 11568, USA*
[2]*Bernard Price Institute for Palaeontological Research, University of the Witwatersrand, Johannesburg 2050, South Africa*
[3]*Bâtiment de Paléontologie, UMR 5143 CNRS, Département Histoire de la Terre, Muséum national d'Histoire naturelle, 8, rue Buffon, F-75008 Paris, France*
[4]*South African Museum, Queen Victoria Street, Cape Town 8000, South Africa*
[5]*Redpath Museum, McGill University, Montreal, Quebec H3A 2K6, Canada*
[6]*Department of Organismal Biology and Anatomy, University of Chicago, Chicago, Illinois 60637, USA*
[7]*Institut de Recherches en Sciences Humaines, Niamey, Niger Republic*

New fossils from the Upper Permian Moradi Formation of northern Niger[1–6] provide an insight into the faunas that inhabited low-latitude, xeric environments near the end of the Palaeozoic era (~251 million years ago). We describe here two new temnospondyl amphibians, the cochleosaurid *Nigerpeton ricqlesi* gen. et sp. nov. and the stem edopoid *Saharastega moradiensis* gen. et sp. nov., as relicts of Carboniferous lineages that diverged 40–90 million years earlier[7–9]. Coupled with a scarcity of therapsids, the new finds suggest that faunas from the poorly sampled xeric belt that straddled the Equator during the Permian period[10–12] differed markedly from well-sampled faunas that dominated tropical-to-temperate zones to the north and south[13–15]. Our results show that long-standing theories of Late Permian faunal homogeneity are probably oversimplified as the result of uneven latitudinal sampling.

For over 150 yr, palaeontologists have understood end-Palaeozoic terrestrial ecosystems largely on the basis of Middle and Late Permian tetrapod faunas from southern Africa. The fauna of these rich beds, particularly South Africa's Karoo Basin, has provided fundamental insights into the origin of modern terrestrial trophic structure[16] and the successive adaptations that set the stage for the subsequent mammalian radiation[13]. A Karoo-like tetrapod fauna has been found across coeval Gondwanan rocks in Brazil, India, Mozambique, Tanzania, Zambia and Zimbabwe. A remarkably similar amniote fauna is known from China, Germany, Laos, Russia and Scotland, although these Laurasian strata host different amphibian groups[9]. The cosmopolitan fauna recorded across Pangaea provides compelling evidence for the unrestricted dispersal of tetrapods during the Middle and Late Permian period. We report here on the discovery of new fossils from West Africa that reveal a highly unusual fauna that has important implications for this interval of vertebrate evolution.

Temnospondyli Zittel, 1888
Edopoidea Romer, 1945

Nigerpeton ricqlesi gen. et sp. nov.

Etymology. *Niger*, for the country, and *herpeton* (Greek), meaning crawler; *ricqlesi*, named for Armand de Ricqlès.

Holotype. MNN MOR69 (Musée National du Niger, Niamey), partial skull and associated atlas vertebra.

Referred material. MNN MOR70, a larger skull preserving most of the left side of the palate, skull roof and lower jaw; MNN MOR83, three isolated sacral neural arches with associated ribs; MNN MOR82, partial femur.

Horizon and locality. Collected from a thin conglomerate in the Upper Permian Moradi Formation, approximately 20 km west of Arlit, north-central Niger.

Diagnosis. Edopoid temnospondyl distinguished from all other edopoids by the unique presence of a highly reduced supratemporal bone, lateral swelling of the maxilla that accommodates two or three fangs medial to the marginal tooth row, maxillary and dentary tooth rows with sporadic appearance of 'doubled' tooth positions, medially positioned premaxillary fangs, and anterior premaxillary vacuities for accommodation of mandibular fangs. Further distinguished from the cochleosaurids *Chenoprosopus* and *Cochleosaurus* by its larger size, extreme preorbital length (~70% of total skull length), anteroposteriorly short skull table, broad sphenethmoid, and the presence of an anterior palatal vacuity.

Saharastega moradiensis gen. et sp. nov.

Etymology. *Sahara*, for the Sahara Desert, and *stege* (Greek), meaning roof; *moradi*, the formation from which the fossil was recovered, and *ensis* (Latin), meaning place or locality.

Holotype. MNN MOR73, nearly complete skull lacking lower jaws.

Horizon and locality. Collected from dark reddish-brown floodplain deposits of the Moradi Formation, approximately 20 km west of Arlit, north-central Niger.

Diagnosis. Distinguished from all other temnospondyls by the unique presence of an extensive tongue-and-groove articulation between the premaxilla and maxilla, and tabulars with exceptionally large, blunt-ended 'horns' that are directed both laterally and ventrally. Further distinguished from all other edopoids by the following unique combination of characters: orbits broadly separated and close to skull margin, pineal foramen absent, basicranial articulation sutural, fossa subrostralis media present, transvomerine tooth row present, palatal tusks highly reduced or absent, supraoccipital ossified.

The Upper Permian Moradi Formation of northern Niger is a 100-m-thick succession of fluvial sediments that were deposited as the result of reactivated strike-slip faults bounding the Izégouan-